On the Exploitation of CubeSats for Highly Accurate and Robust Single-Pass SAR Interferometry

Maxwell Nogueira Peixoto, *Student Member, IEEE*, Gerhard Krieger, *Fellow, IEEE*, Alberto Moreira, *Fellow, IEEE*, Christian Waldschmidt, *Fellow, IEEE*, and Michelangelo Villano, *Senior Member, IEEE*

***Abstract*—Highly accurate digital elevation models (DEMs) from spaceborne synthetic aperture radar (SAR) interferometry are often affected by phase unwrapping errors. These errors can be resolved by the use of additional interferograms with different baselines, but this requires additional satellites in a single-pass configuration, resulting in higher cost and system complexity, or additional passes of the satellites, which affects mission planning and makes the system less suitable for monitoring fast-changing phenomena. This work proposes augmenting a bistatic SAR interferometer with one or more receive-only CubeSats, whose images are used to form an additional interferogram with a small baseline, making the system robust to unwrapping errors. In spite of the lower quality of the CubeSat images due to their small antenna aperture, this additional information can be used to detect and resolve phase unwrapping errors in the DEM without impacting its resolution or accuracy. A processing scheme for the phase unwrapping correction is presented along with a theoretical model for its performance. Finally, a design example is presented and discussed along with a simulation based on TanDEM-X data. It is also shown that CubeSat add-ons allow further increasing the baseline and thus improving the accuracy of DEMs. This concept represents a cost-effective solution for the generation of highly accurate, robust DEMs and paves the way to distributed SAR interferometric concepts based on CubeSats.**

***Index Terms*—Synthetic aperture radar interferometry; CubeSat; Phase unwrapping; TanDEM-X; Bistatic SAR; Multistatic SAR.**

I. Introduction

SYNTHETIC aperture radar (SAR) interferometry is a coherent technique commonly used to extract topographic or motion information through SAR interferograms, which contain the pointwise phase difference between SAR images of the same area taken from different viewpoints or at different times, respectively, [1]-[4]. Across-track SAR interferometry is the case of using SAR images taken from parallel tracks with some separation orthogonal to the azimuth and slant range directions. This separation is called the orthogonal baseline. In this type of interferometry, the interferometric phase is proportional to the terrain height, so a digital elevation model (DEM) can be generated from the data. While the SAR images can be obtained at different times, such as with two passes of a same satellite, the best performance is achieved if the two images are taken simultaneously in a single-pass configuration, as this makes the temporal decorrelation negligible [2]-[5]. The Shuttle Radar Topography Mission (SRTM) and later the TanDEM-X mission used this technique to produce DEMs with unprecedented accuracy [5]-[7]. While SRTM was using a boom to achieve the desired baseline, TanDEM-X consists of two satellites flying in formation and allowed for the generation of a global-scale DEM.

Phase measurements are cyclic, that is, the interferometric phase is only known modulo 2π, so phase unwrapping [8], [9] is required to obtain absolute phase measurements, which can then be converted to heights to form a DEM. In general, phase unwrapping uses the phase continuity assumption, i.e., the assumption that the phase does not change by more than π between neighboring samples, to resolve the 2π ambiguities in the phase values. If this assumption is valid, the phase unwrapping admits a unique solution, but this assumption is often not valid across the entire interferogram, either due to fast-changing terrain topography, such as cliffs or foreshortening areas, or due to phase noise. The phase unwrapping then admits multiple solutions, and a phase unwrapping algorithm can lead to an incorrect one, which is called a phase unwrapping error.

The coefficient of proportionality between the phase and the terrain height is commonly represented by the height of ambiguity, the height change that corresponds to a 2π phase change, and it is inversely proportional to the orthogonal baseline. The uncertainty in the heights of the resulting DEM is related by this coefficient to the uncertainty in the phase measurements, so, the smaller the height of ambiguity, the more accurate the DEM, but also the more likely it is for the phase continuity assumption to be violated and, therefore, for the DEM to contain unwrapping errors. Resolving phase unwrapping errors is therefore essential for DEM generation.

Phase unwrapping errors can be resolved if one or more

Manuscript received MMMMM DD, YYYY; accepted MMMMM DD, YYYY. Co-funded by the European Union (ERC, DRITUCS, 101076275). Views and opinions expressed are however those of the authors only and do not necessarily reflect those of the European Union or the European Research Council Executive Agency. Neither the European Union nor the granting authority can be held responsible for them. This work was partially funded by the Deutsche Forschungsgemeinschaft (DFG, German Research Foundation) GRK 2680 – Project-ID 437847244. (Corresponding author: Maxwell Nogueira Peixoto.)

Maxwell Nogueira Peixoto, Gerhard Krieger, Alberto Moreira, and Michelangelo Villano are with the German Aerospace Center (DLR), Microwaves and Radar Institute Oberpfaffenhofen, 82234 Wessling, Germany (e-mail: maxwell.nogueirapeixoto@dlr.de).

Christian Waldschmidt is with the Ulm University, Institute for Microwave Engineering, Albert-Einstein-Allee 41, 89081 Ulm, Germany (e-mail: christian.waldschmidt@uni-ulm.de).

Digital Object Identifier XXXXXXXXXXXXXXX

additional interferograms from the same area, but with different baselines, are available [10], [11]. One possibility of achieving this is through a multistatic system with three or more receiver satellites with large antenna apertures [11]. The drawback of this approach is the increased system complexity and cost. Another possibility is to use a bistatic system but perform two or more acquisitions over the same area with different baselines on different passes of the satellites. This is the strategy employed by TanDEM-X [10]. With this approach, however, orbit maneuvers are necessary to change the baseline for the additional passes, and the system cannot be used to robustly monitor fast-changing phenomena. The solution proposed in this work is to add one or more receive-only CubeSats flying in formation with a large-baseline bistatic SAR interferometer, e.g., like TanDEM-X. SAR missions using CubeSat platforms are promising low-cost solutions for remote sensing [12]-[15]. The CubeSat add-on proposed in this work allows forming an additional small-baseline interferogram that can be used for resolving the phase unwrapping errors in spite of its lower quality caused by the increased noise and ambiguity levels in the CubeSat images [16].

This work is organized as follows: Section II presents two possible configurations of the concept and their characteristics; Section III discusses how the additional information provided by the CubeSat add-on can be used to resolve phase unwrapping errors; Section IV assesses the theoretical performance of the phase unwrapping correction procedure; and Section V shows a design example of the proposed CubeSat add-on along with a simulation of the system based on TanDEM-X data [5].

II. System Configurations

The proposed system consists of a bistatic SAR interferometer formed by two satellites, called the main satellites, one or two of which are responsible for transmitting pulses[1], along with one or more CubeSat receivers with small antenna apertures, whose images are used to form a small-baseline interferogram that serves to correct phase unwrapping errors. An additional medium-baseline interferogram can also be formed that, as will be shown in Section III, serves to detect unwrapping errors, and such information can be used to skip the unwrapping correction on areas without unwrapping errors.

Nested helix orbits [17], [18] are used for the formation flight of the main satellites with the CubeSat add-on. Without loss of generality, the orbit of the main satellite number 1 is assumed as reference and the other satellites describe helix orbits around it. Two configurations are proposed for the arrangement of the CubeSat add-on. In the first, shown in Fig. 1 (a), a single CubeSat is added flying in formation with the main satellites and forming a small baseline with one of them. The small-baseline interferogram is then formed from the images of the CubeSat and the closest main satellite. The helix followed by the CubeSat is in phase with that of the main satellite number 2, but its maximum radial and horizontal baselines are smaller by the same factor. This formation guarantees an approximately fixed ratio of the large to the small orthogonal baseline across the whole orbital period. A fixed baseline ratio is desirable, as this ratio drives the performance of the phase unwrapping correction. Additionally, exclusion zones can be used to avoid that one of the satellites illuminates the others and damage their electronics. This solution is also adopted in TanDEM-X [19]. This configuration offers the best unwrapping correction performance. A second configuration, shown in Fig. 1 (b), foresees instead two CubeSats flying in close formation with a small baseline between themselves and with some separation (e.g., an along-track separation) from the main satellites. The small-baseline interferogram is then formed from the images of the two CubeSats. The helixes followed by the CubeSats are again in phase with that of the main satellite 2, but with scaled maximum radial and horizontal baselines. By keeping the CubeSats separate from the main satellites, this second configuration more easily meets formation flight safety requirements and avoids maintaining a CubeSat in close formation flight with much larger satellites, which is a challenge due to the former experiencing a different drag than the latter.

Three interferograms are formed from the SAR images after coregistration:

- the large-baseline interferogram, formed from the images of the main satellites;
- the small-baseline interferogram, formed, in the first configuration, from the images of the CubeSat and one of the main satellites, and, in the second configuration, from the images of the two CubeSats;
- the medium-baseline interferogram, formed, in the first configuration, from the images of the CubeSat and the other main satellite, and, in the second configuration, by combining the large- and small-baseline interferograms through simple pointwise multiplication of the complex samples of one by the conjugate of the complex samples of the other. As noted in [10], for better performance, this pointwise multiplication should be done after multilooking the large- and small-baseline interferograms.

[1] In the following, we assume without lack of generality that just one of the main satellites is transmitting. If both satellites are used for transmission, the transmit event is switched from pulse to pulse between the satellites (the so-called alternating transmit mode) [5]. Please note that the alternating transmit mode generates two interferograms with full- and half-sized baselines from the images of the main satellites, and more than one small- and medium-baseline interferograms from the images of the CubeSats and the main satellites, all of which can be also used for improving phase unwrapping. However, the alternating transmit mode implies halving the swath width as a consequence of the transmit pulse switching, i.e. the total PRF is doubled, so the receive window length is halved.

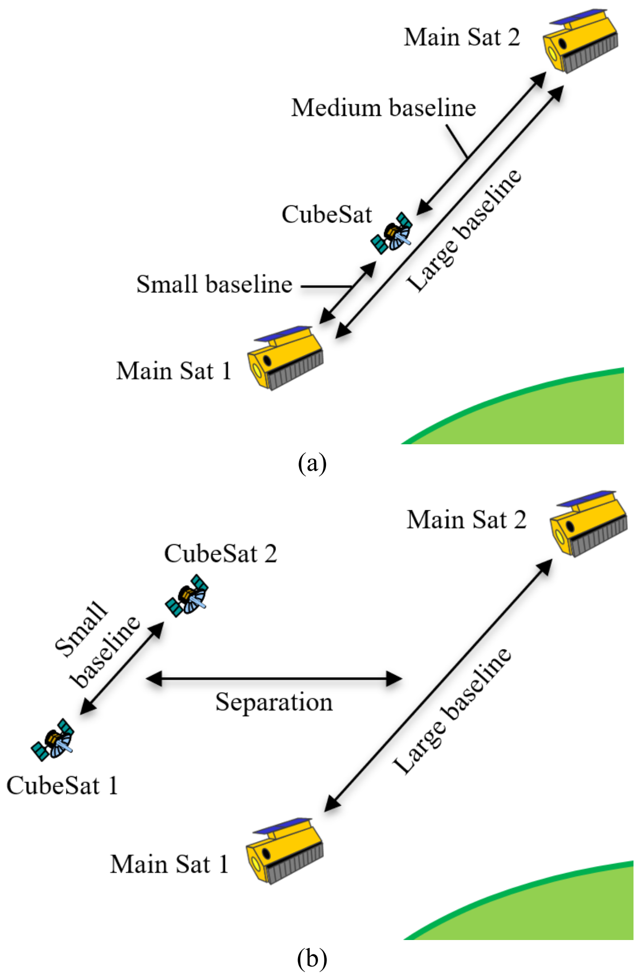

Fig. 1. Proposed configurations for the CubeSat add-on. In the first configuration (a), a single CubeSat flies in close formation with the main satellites, possibly with some along-track separation, and in the second configuration (b) two CubeSats fly in close formation with each other, but with a significant separation (e.g., an along-track separation) from the main satellites.

The main challenge of this concept is that CubeSats are characterized by very small antenna apertures. One consequence of such is a wider antenna pattern, which causes elevated range and azimuth ambiguities. Note that the CubeSats are receivers, so ambiguity suppression is still provided by the transmit antenna pattern of one of the main satellites. Another consequence of the small antenna aperture is a lower antenna gain, which causes lower signal-to-noise ratio (SNR). Both the lower SNR in the CubeSat images and their increased range and azimuth ambiguity levels cause increased decorrelation of the small- and medium-baseline interferograms, with the SNR decorrelation being the most impactful. Moreover, the azimuth ambiguity levels can introduce biases into these interferograms [20]. These effects on the interferograms are stronger in the second configuration, shown in Fig. 1 (b), because two CubeSat images are used to form them, whereas in the first configuration, shown in Fig. 1 (a), only one CubeSat image is used and the other image is from a main satellite, which does not have a small aperture.

There are different options for addressing the synchronization between the CubeSats and the main satellites. One option is the MirrorSAR concept [21], that achieves synchronization by demodulating the echoes received by the CubeSats using either the oscillator of the main satellite which transmitted the pulse or the oscillator of the other main satellite, which is synchronized to the former. This is possible by designing the CubeSats as transponders that forward the echoes they receive to one of the main satellites, possibly through an optical link. Another option is to employ a GNSS-based synchronization scheme [22], as planned for ESA's Harmony mission [23], where the GNSS receiver shares the same oscillator as the radar and so allows the GNSS carrier to be used as a reference for correcting the oscillator errors. A dedicated synchronization link, as implemented in TanDEM-X by the exchange of pulses [5], [24], could also be used. Additionally, data-based synchronization techniques [25] could be employed, also in combination with other synchronization schemes.

The orbit maintenance of the CubeSats requires fuel consumption and CubeSats can have very strict fuel capacity constraints due to their small size. The CubeSats, however, experience much less drag than the main satellites due to the size difference, and therefore have proportionately less fuel consumption. Even so, the ratio between the fuel capacity and the drag can be lower for the CubeSats than for the main satellites, causing the orbit maintenance to deplete the fuel of the former earlier than the fuel of the latter, assuming the same specific impulse for the thrusters in both. A promising technology for addressing this is electric propulsion for the CubeSats, which achieves a much higher specific impulse than conventional chemical thrusters [26], [27]. Because of the lower cost of the CubeSats, another possibility is to accept their lower lifetime and replace them with other CubeSats when needed.

III. Processing and Phase Unwrapping Correction

A processing scheme based on the TanDEM-X dual-baseline phase unwrapping framework [10] is proposed for utilizing the additional information provided by the CubeSats to detect and correct unwrapping errors. The large-, medium- and small-baseline interferograms are independently multilooked and unwrapped, forming three DEMs. Unwrapping errors are detected by comparing the height of the large-baseline DEM with those of the medium- and small-baseline DEMs, and the small-baseline DEM is used as a reference to correct them.

The phase unwrapping correction is performed pixelwise in the coregistered slant-range geometry, i.e., prior to geocoding, and under the assumption that the small-baseline DEM is free of unwrapping errors due to its large height of ambiguity. The correction therefore consists of adding or subtracting a multiple of the height of ambiguity to the large-baseline DEM height h_L that makes the result as close as possible to that of the small-baseline DEM height h_S:

$$h_{\text{final}} = h_L + \left\lfloor \frac{h_S - h_L}{HoA_L} \right\rceil HoA_L, \tag{1}$$

where h_{final} is the corrected height, HoA_L is the height of ambiguity of the large-baseline DEM, and $\lfloor \cdot \rceil$ is the operation of rounding to the nearest integer. Due to the variance of the height from the large- and small-baseline DEMs and the presence of biases, it is possible that this unwrapping correction adds or subtracts an incorrect multiple of the height of ambiguity, so that the final DEM height h_{final} contains unwrapping errors with respect to the true terrain height. These are called residual unwrapping errors and they will be discussed further in Section IV.

To avoid introducing residual unwrapping errors in the areas where the large-baseline DEM was unwrapped correctly, the phase unwrapping correction described in (1) is only performed on areas where unwrapping errors are detected. The unwrapping errors can be detected by comparing the large-baseline DEM with the medium-baseline DEM, similarly to how it is done in TanDEM-X [10]. To eliminate false negatives, i.e., when the DEMs contain equivalent unwrapping errors which are then not detected, the large-baseline DEM is further compared to the small-baseline DEM. These detections are first done pixelwise, and then processed for smoothing and rejection of false detections. This approach is effective because unwrapping errors generally occur uniformly over large areas.

Initially, the difference between the heights h_L and h_M of, respectively, the large- and medium-baseline DEMs is pixelwise compared to a threshold, such that exceeding it is indicative of unwrapping errors. To avoid false detections, this threshold must be sufficiently larger than the variance of the height difference, although elevated rates of false-detections are acceptable because most are later removed in the process of smoothing the mask, and, even if they are not, they cause little impact on the final DEM. The recommended value for this threshold is the difference between the corresponding heights of ambiguity:

$$|h_L - h_M| \geq |HoA_L - HoA_M|, \tag{2}$$

which is the bias present when both DEMs have matching unwrapping errors equal to one height of ambiguity (cf. Fig. 2).

This procedure fails to detect unwrapping errors if the biases caused by them are equal or almost equal between the large- and medium-baseline DEMs. For example, as illustrated in Fig. 2, with heights of ambiguity of 20 m and 30 m and unwrapping errors of 3 and 2 heights of ambiguity, both DEMs would be offset by 60 m, and no bias would be present in the height difference. These false negatives are characterized by large height offsets (usually at least $3HoA_L$), and so can be detected by further comparing the large-baseline DEM with the small-baseline DEM. This is also done by pixelwise comparing the height difference against a threshold, whose recommended value is the minimum unwrapping error offset in the large-baseline DEM that could cause a false negative in the comparison with the medium-baseline DEM (2):

$$|h_L - h_S| \geq n_L HoA_L, \tag{3}$$

where n_L is the minimum positive integer such that

$$|n_L HoA_L - n_M HoA_M| \ll |HoA_L - HoA_M| \tag{4}$$

for some integer n_M.

Note that (1) and the thresholds in (2) and (3) all depend on the heights of ambiguity, which are variant across the image. This can be easily accounted for in the processing because the corresponding unwrapping correction and thresholding operations are performed pixelwise.

Due to the pixelwise nature of the unwrapping error detection scheme, the resulting mask appears "noisy" in the regions where the biases in the height differences are close to the thresholds for detection. Sporadic false detections may also be present. A further processing step is needed to reject the sporadic false detections and smooth the "noisy" areas into areas with uniform detection. The proposed method is to use the DBSCAN clustering algorithm [28] on the pixelwise detection mask. For every pixel where an unwrapping error is detected, the region with a radius ε centered on that pixel is called its Eps-neighborhood, and the pixel is classified either as a core or a border or a noise pixel according to the following rules: if there are at least $n_{\min}$ other pixels with detections inside this Eps-neighborhood, the pixel is classified as a core pixel; if the pixel is not a core pixel but contains a core pixel in its Eps-neighborhood, it is classified as a border pixel; otherwise, the pixel is classified as noise pixel. The output detection mask is then formed by including all core and border pixels and all pixels within their respective Eps-neighborhoods. This process rejects detections which are locally sparse (noise pixels) and accepts and smooths areas with detection which are locally dense (core and border pixels). The radius ε of the Eps-neighborhoods and the minimum number of neighbors $n_{\min}$ for classification as a core pixel are the two parameters of the algorithm. The scale for locality is defined by ε and the density threshold for acceptance is $n_{\mathbf{min}}$ detections over the area of the Eps-neighborhood. Using (2) and (3), the pixelwise probability of unwrapping error detection is at worst about 50%[2], which occurs when the detection threshold is at the mean of the probability density function of the height difference (cf. Fig. 2 (b)). For this reason, the two parameters should be chosen such that the density threshold of the DBSCAN is sufficiently lower than 50%.

[2] The pixelwise probability of unwrapping error detection can be worse than 50% if there are strong biases caused by coherent azimuth ambiguities.

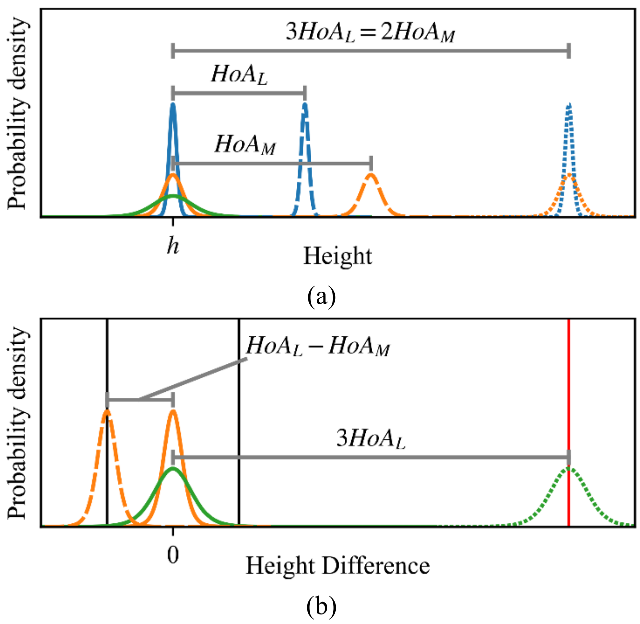

Fig. 2. Probability density functions of (a) the height in the large- (blue), medium- (orange), and small- (green) baseline DEMs, and (b) the height difference between the large-baseline DEM and the medium- (orange) and small- (green) baseline DEMs for an exemplary SAR interferometer with the CubeSat add-on. The terrain height is denoted by h. The continuous curves represent the case of no unwrapping errors. The dashed curves represent the case of unwrapping errors equal to one height of ambiguity in the large- and medium-baseline DEMs, which are detected by comparison of the height difference between them with the recommended threshold (cf. (2)), indicated by the black vertical lines in Fig. 2 (b). The dotted curves represent the case of unwrapping errors resulting in equal biases in the large- and medium-baseline DEMs, which cannot be detected by their height difference and are instead detected by comparison of the height difference between the large- and small-baseline DEMs with the recommended threshold (cf. (3)), indicated by the red vertical line in Fig. 2 (b).

In the proposed scheme, the height estimates that compose the final DEM are derived directly from the large-baseline interferogram, formed from images of the main satellites, and the additional information provided by the CubeSats is used for correcting unwrapping errors. One could additionally consider incorporating the CubeSat images in the height estimation to achieve a better height accuracy, for example, using the maximum-likelihood multi-baseline height estimation [29], [30]. However, the achieved accuracy gain is often very small as the CubeSat images have increased noise and do not form large baselines with the other satellites. Additionally, with joint processing, artifacts present in the low-quality CubeSat images such as strong azimuth ambiguities could corrupt the final DEM. The proposed approach avoids this by "isolating" the CubeSat images to their use in the unwrapping correction. With the proposed processing scheme, the final DEM has the same resolution and height uncertainty as the large-baseline DEM, i.e., the CubeSat add-on does not directly alter the performance of the system aside from providing robustness to unwrapping errors. Even so, this robustness to unwrapping errors allows the main interferometer to operate with a larger baseline and, therefore, higher accuracy than what would otherwise be feasible without the add-on. Finally, because unwrapping errors generally appear uniformly over large regions, it is acceptable to trade the resolution of the medium- and small-baseline DEMs in order to improve other aspects of the system. One possibility of exploiting this is to increase the number of looks in the small-baseline interferogram to decrease its height variance and, therefore, decrease the probability of residual unwrapping error. Another possibility is to utilize a lower bandwidth in the CubeSats, which would also reduce the volume of data to be downlinked, but at the same time would lead to a loss of quality of the small-baseline DEM.

IV. Performance

The performance of the CubeSat add-on can be evaluated in terms of its effectiveness in correcting unwrapping errors in the final DEM. This section discusses this performance and how it relates to the heights of ambiguity, the numbers of looks, and the interferometric coherences, which in turn depend on system parameters such as the sizes of the antennas. The other performance parameters of the final DEM such as resolution and height accuracy are, in general, not directly dependent on the information provided by the CubeSat add-on. They depend only on the characteristics of the large-baseline interferogram, and will, therefore, not be discussed.

In a SAR interferometer with the proposed CubeSat add-on, unwrapping errors are either residual unwrapping errors, i.e., errors caused by the unwrapping correction described in (1) adding or subtracting an incorrect multiple of the height of ambiguity, or false negatives in the unwrapping error detection mask. The variance of the height indicated by the small-baseline DEM is large due to its large height of ambiguity and the lower coherence of the corresponding interferogram. Residual unwrapping errors are caused by this height variance and also by biases in the small-baseline DEM due to various causes such as strong coherent ambiguities [20], smaller resolution because of the larger number of looks, or unwrapping, coregistration, synchronization and baseline estimation errors. Note that biases due to strong coherent azimuth ambiguities can be mitigated by employing a slight variation of the pulse repetition interval [31].

The probability that a residual unwrapping error occurs, i.e., the probability that the corrected height h_{final} as described in (1) differs from the true height of terrain h by more than half of the height of ambiguity, is the probability that

$$|\varepsilon_S - \varepsilon_L| > \frac{HoA_L}{2}, \tag{5}$$

where

$$\varepsilon_S = h_S - h \tag{6}$$

is the error in the height of the small-baseline DEM h_S with respect to the true height of the terrain h,

$$\varepsilon_L = h_L - h - \left\lfloor \frac{h_L - h}{HoA_L} \right\rceil HoA_L \tag{7}$$

is the error in the height of the large-baseline DEM h_L with respect to the true height of the terrain h after discounting any unwrapping errors in h_L, and HoA_L is the height of ambiguity of the large-baseline DEM. Although ε_S and ε_L are not statistically independent, the assumption of independence (also made in [32]) yields a good approximation of the probability of residual unwrapping error that is much easier to compute:

$$P\left(|\varepsilon_S - \varepsilon_L| > \frac{HoA_L}{2}\right) \cong 1 - \int_{-\frac{HoA_L}{2}}^{\frac{HoA_L}{2}} (p_{\varepsilon_L} \star p_{\varepsilon_S})(\varepsilon) d\varepsilon, \tag{8}$$

where $\star$ is the cross-correlation operator, and p_{ε_L} and p_{ε_S} are the probability density functions of ε_L and ε_S, respectively (cf. Fig. 3). The usual model for these probability distributions is derived from the model of the probability distribution of the interferometric phase described in [2], [33], [34] scaled by the corresponding height of ambiguity. This model has the height of ambiguity, the interferometric coherence and the number of looks as parameters, and can also be adapted by simple translation to include the bias caused by coherent azimuth ambiguities [20]. The coherence, in turn, can be expressed as product of many terms: the SNR, quantization, baseline, azimuth spectral shift and misregistration, volume, and temporal decorrelations, and the coherence change caused by range and azimuth ambiguities. The modelling of these terms is well established in the literature [5], [20], [35], but special attention is given to the volume decorrelation due to its dependence on the height of ambiguity, and to the SNR decorrelation and the effect on the coherence caused by coherent azimuth and range ambiguities [20] because, in the small-baseline interferogram, they are related to the size and shape of the CubeSat antennas.

Fig. 4 shows the probability of residual unwrapping error as a function of the coherences of the large- and small-baseline interferograms with 25 and 49 looks, respectively, and a height-of-ambiguity ratio of 3.5. With these parameters, a probability of residual unwrapping error of about 0.5% is achieved with the very low coherence of 0.35 in the small-baseline interferogram. It can also be observed that the coherence of the large-baseline interferogram has very little impact on the probability of residual unwrapping error. The reason for that is that the small-baseline interferogram has a much larger height of ambiguity than the large-baseline one, so the variance of the corresponding height error ε_S is much larger than that of the large-baseline DEM ε_L.

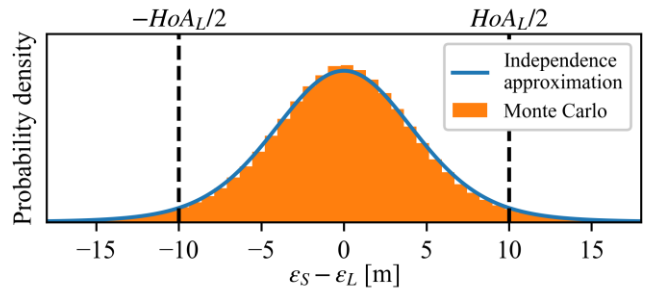

Fig. 3. Probability distribution of $\varepsilon_S - \varepsilon_L$ (cf. (5), (6) and (7)) obtained from a Monte Carlo simulation (orange bars) and the one resulting from assuming ε_S and ε_L to be independent (blue line) for an exemplary system in the first configuration (cf. Fig. 1 (a)) with heights of ambiguity of 20 m and 70 m, coherences of 0.5 and 0.25, and 25 and 49 looks for the large- and small-baseline interferograms, respectively, and a coherence of 0.25 for the medium-baseline interferogram.

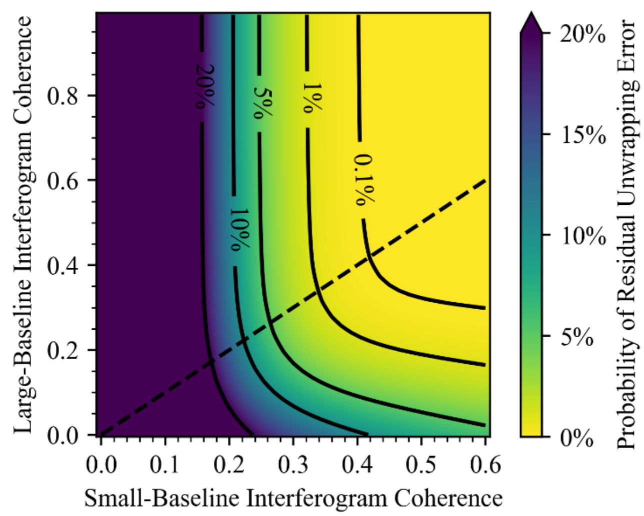

Fig. 4. Probability of residual unwrapping error computed according to (8) as a function of the coherences of the large- and small-baseline interferograms considering that 25 and 49 looks, respectively, are used, and that the height of ambiguity of the small-baseline interferogram is 3.5 times larger than that of the large-baseline one. The black dashed line marks where both coherences are equal.

Note, however, that the coherences of the large- and small-baseline interferograms are linked, as they refer to the same areas, but observed with different noise levels and heights of ambiguity, so, although a change in the coherence of the large-baseline interferogram does not affect the probability of residual unwrapping error by itself, it comes with a corresponding change in the coherence of the small-baseline one, which does affect the probability of residual unwrapping error. For example, the relation between the SNR decorrelation in the large- and small-baseline interferograms, $\gamma_{SNR\,L}$ and $\gamma_{SNR\,S}$, respectively, is given, for the CubeSat add-on in the first configuration (cf. Fig. 1 (a)) and under the assumption that the two main satellites have the same noise-equivalent sigma naught (NESN) [36], by:

$$\gamma_{SNR\,S} = \frac{\gamma_{SNR\,L}}{\sqrt{\gamma_{SNR\,L} + (1-\gamma_{SNR\,L}) \cdot \frac{NESN_{\text{cubesat}}}{NESN_{\text{main}}}}}, \tag{9}$$

where $NESN_{\text{main}}$ and $NESN_{\text{cubesat}}$ are the NESN for the main satellites and the CubeSat, respectively. This relation is derived by combining the expressions for the two SNR decorrelations [2], [35] assuming that the SNRs of the main satellites and the CubeSat are the ratio between a common sigma naught and their respective NESN. The larger the large-baseline SNR decorrelation, the larger the small-baseline one, with the latter always being stronger due the higher NESN of the CubeSat images.

A second aspect of the link between the coherences is the volume decorrelation present in volume scattering scenarios, such as forests. It depends on the height of ambiguity and so on the baseline and, in general, the smaller the baseline, the weaker it is [2], [5], so the volume decorrelation is in general weaker in the small-baseline interferogram than in the large-baseline one. This is advantageous to the phase unwrapping correction because, as previously discussed and also shown in Fig. 4, the coherence of the former is much more relevant to the probability of residual unwrapping error than the coherence of the latter. For example, using the model of an exponential vertical reflectivity profile, the relation between the large- and small-baseline volume decorrelations, $\gamma_{vol\,L}$ and $\gamma_{vol\,S}$, is given by:

$$\gamma_{vol\,S} = \sin\arctan\left(\frac{HoA_S}{HoA_L}\tan\arcsin\gamma_{vol\,L}\right), \tag{10}$$

where HoA_L and HoA_S are the heights of ambiguity of the large- and small-baseline interferograms, respectively.

The larger the height of ambiguity of the small-baseline DEM, the more robust it is to unwrapping errors, but also the larger the variance of ε_S and so, for a same coherence, the larger the probability of residual unwrapping error, as Fig. 5 shows. Note, however, that if significant volume scattering is present, the volume decorrelation weakens with increasing height of ambiguity, which can instead decrease the variance of ε_S and decrease the probability of residual unwrapping error. Similarly, the larger the number of looks used in the small-baseline DEM, the smaller the variance of ε_S and so the smaller the probability of residual unwrapping error, as Fig. 6 shows. Note also that the probability of unwrapping error, all else being equal, depends on the ratio between the heights of ambiguity and not on their absolute values. While the heights of ambiguity can change significantly across the swath due to their dependence on the incidence angle, the ratios between them generally do not change much, so the range dependence of the unwrapping correction performance is derived primarily from the range dependence of the coherences.

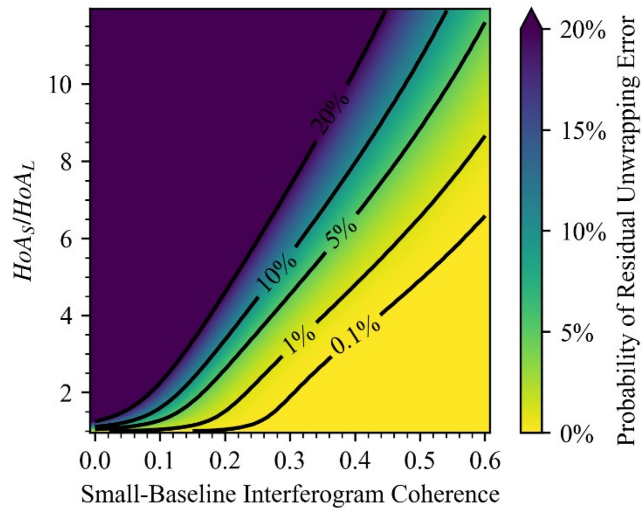

Fig. 5. Probability of residual unwrapping error computed according to (8) as a function of the coherence of the small-baseline interferogram and the ratio between the heights of ambiguity of the small- and large-baseline interferograms, considering that 49 and 25 looks, respectively, are used, and that the coherence of the large-baseline interferogram is 0.8.

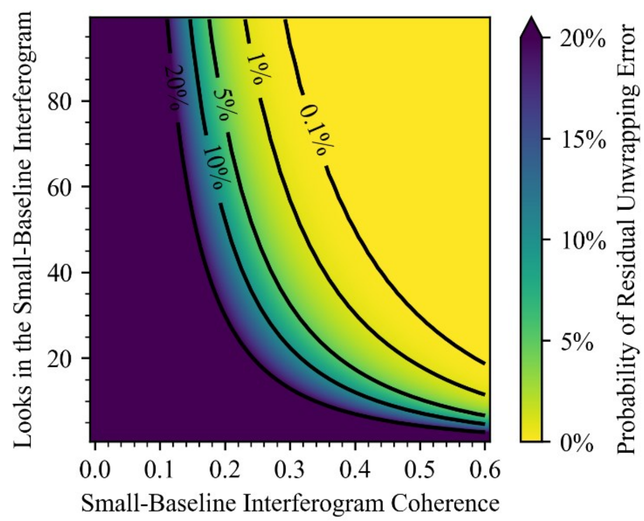

Fig. 6. Probability of residual unwrapping error computed according to (8) as a function of the coherence of the small-baseline interferogram and the number of looks used for it, considering the coherence of the large-baseline interferogram to be 0.8 and that 25 looks are used for it.

The other relevant parameter is the bias present in the small-baseline DEM, which can be caused by strong coherent azimuth ambiguities [20], errors in the estimation of the small-baseline height of ambiguity, and synchronization errors. As shown in Fig. 7, the stronger the bias, the lower the probability of residual unwrapping error. However, relatively large biases in the small-baseline DEM (larger than what would be acceptable in the large-baseline interferogram and, so, in the final DEM) still result in acceptable probabilities of residual unwrapping errors. As shown in Fig. 7, a probability of residual unwrapping error lower than 1% is achieved for any bias up to around 20% of the height of ambiguity of the large-baseline interferogram, considering that the height of ambiguity of the small-baseline interferogram is 3.5 times larger than that of the large-baseline one, and that, respectively, the coherences are 0.42 and 0.8, and 49 and 25 looks are used.

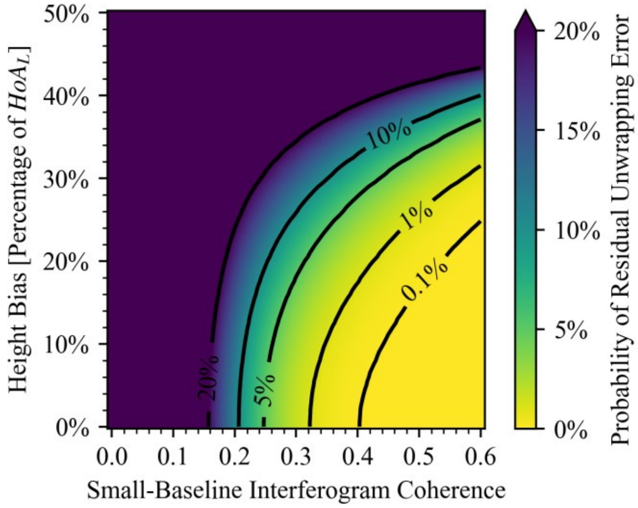

Fig. 7. Probability of residual unwrapping error computed according to (8) as a function of the coherence of the small-baseline DEM and the height bias present in it, considering that the coherence of the large-baseline interferogram is 0.8, that the height of ambiguity of the small-baseline interferogram is 3.5 times larger than that of the large-baseline one, and that 25 and 49 looks are used for the large- and small-baseline interferograms, respectively.

In SAR interferometry, a very accurate knowledge of the baseline, which is then used to estimate the height of ambiguity, is required. A baseline estimation error causes a bias in the DEM proportional to the error and inversely proportional to the baseline. Consequently, for a same baseline estimation accuracy, the height bias in the small-baseline DEM is more pronounced than in the large-baseline DEM. However, because the small-baseline DEM is used for the unwrapping correction, it is more tolerant to heights biases, accepting biases up to around 20% of the large-baseline height of ambiguity (cf. Fig. 7). Furthermore, if the baseline estimation accuracy for the CubeSat is not sufficient, one could attempt to refine the estimation of the height of ambiguity of the small-baseline interferogram though a data-based approach that matches small-baseline interferogram to the large-baseline one, since both correspond to the same underlying topography.

Finally, the probability of residual unwrapping error can be linked to the size and shape of the antennas of the CubeSats through the noise and azimuth and range ambiguity levels. The NESN of the CubeSat images is linearly dependent on the effective area of the respective CubeSat antenna, and, the higher the NESN, the stronger the SNR decorrelation in the small-baseline interferogram (cf. (9)) and so the higher the probability of residual unwrapping error (cf. Fig. 4). The smaller the antennas of the CubeSats, the wider the antenna pattern and so the stronger the range and azimuth ambiguity levels and the stronger the biases and the effect on the coherence of the small-baseline interferogram caused by them as described in [20], which in turn decrease the probability of residual unwrapping error (cf. Fig. 4 and Fig. 7). This link between the area of the antennas of the CubeSats and the probability of residual unwrapping error can then be used in the system design to translate requirements of maximum probability of residual unwrapping error into requirements of minimum antenna area, as will also be exemplified in Section V.A.

V. Design Example based on TanDEM-X

In this section, a design example based on TanDEM-X with a CubeSat add-on in the first configuration (cf. Fig. 1 (a)) is discussed along with a simulation based on TanDEM-X data. The parameters of the system are shown in Table I. The case of heights of ambiguity of 20 m and 70 m for the large- and small-baseline interferograms, respectively, is considered. The baseline between the CubeSat and the closest main satellite is 164 m and is larger than the minimum baseline required for safe formation flight in TanDEM-X [6]. Note that the height of ambiguity of the large-baseline interferogram is much smaller than the typical 30 m to 35 m used in TanDEM-X [5]. This results in a higher accuracy of the final DEM unless there is significant volume scattering, and is possible because of the robustness to unwrapping errors provided by the CubeSat add-on.

The mass and frontal area reported for the CubeSat in Table I are rough estimates considering a 12U CubeSat. The fuel consumption required for obit maintenance is inversely proportional to the thruster's specific impulse and proportional to the drag experienced by the satellite, which is proportional to its frontal area. Assuming that the same fuel and thruster type is used in the CubeSat and the main satellites, the fuel consumption for the CubeSat orbit maintenance can be estimated as, by the ratio of the respective frontal areas, 1.6% of the consumption of one of the main satellites. The mass of fuel to be carried by the CubeSat so that it has the same lifetime as the main satellites can then be roughly estimated by scaling by this factor the mass of fuel carried by each main satellite, resulting in about 1.8 kg. Electric propulsion for the CubeSat is a promising technology that can significantly reduce this required fuel mass by achieving a much higher specific impulse than conventional chemical propulsion [26], [27]. Alternatively, due to its lower cost, the CubeSat could be launched with a lower fuel mass and be replaced by another when the fuel is depleted.

TABLE I
PARAMETERS OF THE DESIGN EXAMPLE

Orbit height		514 km
Incidence angle		36.2°
Central frequency		9.65 GHz
Chirp bandwidth		100 MHz
Sampling frequency		110 MHz
PRF		3200 Hz
Processed Doppler bandwidth		2750 Hz
Main satellites	Antenna	rectangular, 4.8 m (length) 0.7 m (height)
	Noise-equivalent beta naught [36]	−21.9 dB
	Azimuth-ambiguity-to-signal ratio	−17.4 dB
	Total mass	1341 kg [37]
	Fuel mass	114 kg [37]
	Frontal area	3.1 m² [37]
CubeSat	Antenna	square, 0.5 m
	Noise-equivalent beta naught [36]	−10.6 dB
	Azimuth-ambiguity-to-signal ratio	−8.1 dB
	Total mass	15 kg
	Frontal area	0.05 m²
Large-baseline interferogram	Orthogonal baseline	573 m
	Height of ambiguity	20 m
	Number of looks	25
Medium-baseline interferogram	Orthogonal baseline	409 m
	Height of ambiguity	28 m
	Number of looks	49
Small-baseline interferogram	Orthogonal baseline	164 m
	Height of ambiguity	70 m
	Number of looks	49

A. Performance Analysis and CubeSat Antenna Size Selection

First, the relation between the probability of residual unwrapping error and the size of the CubeSat antenna is discussed. The analysis is then extended to show the impact of volume decorrelation and strong azimuth ambiguities. These analyses are used for defining the area of the CubeSat antenna and can be further extended to impose requirements on other error sources, such as coregistration and synchronization errors.

Fig. 8 shows the probability of residual unwrapping error for the system as a function of the CubeSat antenna area and the SNR of the SAR images acquired by the main satellites, ignoring at first range and azimuth ambiguities, which will be considered at a later stage. The figure is built using (8) with the conventional model for the height error [2], [33], [34]. The coherences of the large- and small-baseline interferograms are computed by multiplication of the SNR decorrelation for different backscatter levels by a noise- and ambiguity-free coherence of 0.93. This leads to a coherence of 0.8 in the large-baseline interferogram for a beta naught of −14.1 dB, the 5th percentile of the backscatter for soil and rock at X band and HH polarization from the model presented in [38]. The figure shows that a CubeSat with a 50 cm square antenna added to a TanDEM-X-like system leads to a probability of residual unwrapping error smaller than 0.1% for any soil and rock backscatter in the 90% occurrence interval [38]. Similar results would of course be achieved with a reflector antenna of equivalent size.

In volume scattering scenarios, such as forested areas, significant volume decorrelation is present, which impacts the probability of residual unwrapping error. However, as shown in Fig. 4, the coherence of the small-baseline interferogram is much more relevant to the probability of residual unwrapping error than that of the large-baseline one, and the volume decorrelation in the former is much weaker than in the latter due to the larger height of ambiguity [39], so the impact of the volume scattering is reduced. Fig. 9 shows the probability of residual unwrapping error as a function of the volume decorrelation in the small-baseline interferogram and the SNR in the images of the main satellites considering the same parameters as in Fig. 8, a CubeSat with a 50 cm square antenna, and a volume decorrelation of 0.4 for the large-baseline interferogram, matching the reported in [39] for a test area in the Amazon rainforest and the 20 m height of ambiguity of the large-baseline interferogram. The figure shows that a probability of residual unwrapping error smaller than 1% is achieved for any tree backscatter in the 90% occurrence interval [38] and volume decorrelations until around 0.77, which approaches the volume decorrelation reported in [39] for the 70 m height of ambiguity of the small-baseline interferogram.

The analysis can be extended to consider the effect of strong coherent azimuth ambiguities, which is discussed in [20] and depends on the local ambiguity-to-signal ratio (ASR) of the images and the difference between the interferometric phases of the main and ambiguous components. The average probability of residual unwrapping error across these phase differences is shown in Fig. 10 as a function of the local ASR and SNR in the images of the main satellites and assuming the CubeSat to have a 50 cm square antenna. Furthermore, the noise-free coherence of the ambiguities is considered to be 0.93, the same as that of the main component, and the local ASR of the CubeSat images is considered to be proportionally higher than that of the images of the main satellites according to their respective distributed-target azimuth-ambiguity-to-signal ratio (AASR) derived from the two-way antenna patterns. In this scenario, the distributed-target AASRs are −17.4 dB and −8.1 dB for images of the main satellites and the CubeSat, respectively, and Fig. 10 shows that the average probability of residual unwrapping error is still below 1% for local ASRs up to around 7 dB larger than that.

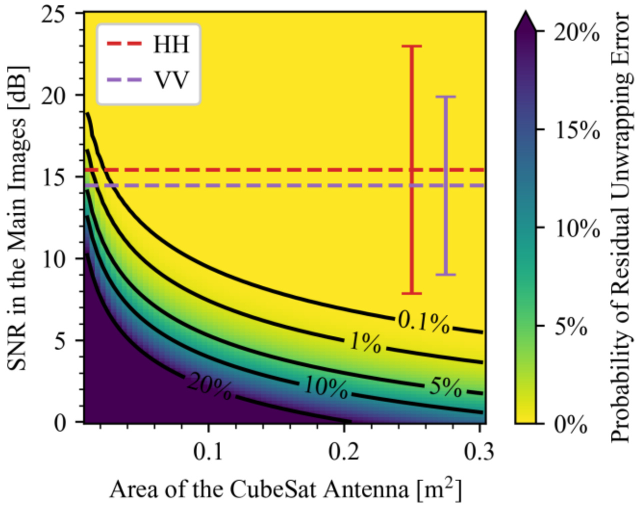

Fig. 8. Probability of residual unwrapping error as a function of the area of a square CubeSat antenna and the SNR in the images of the main satellites for the system described in Table I with a CubeSat add-on in the first configuration (cf. Fig. 1 (a)). The horizontal dashed lines and associated error bars mark the SNR corresponding to the mean and 90% occurrence interval of the backscatter from soil and rock at X band for the (red) HH and (purple) VV polarizations according to the model presented in [38]. The absence of range or azimuth ambiguities is assumed along with a noise-free coherence of 0.93, which corresponds to 0.8 coherence in the large-baseline interferogram at the indicated 5th percentile backscatter at HH polarization.

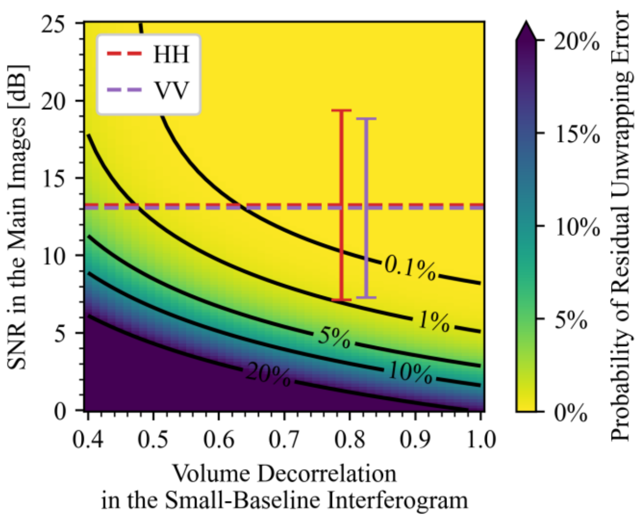

Fig. 9. Probability of residual unwrapping error as a function of the volume decorrelation in the small-baseline interferogram and the SNR in the images of the main satellites for the same parameters as in Fig. 8, but considering a CubeSat with a 50 cm square antenna and a volume decorrelation of 0.4 in the large-baseline interferogram. The horizontal dashed lines and associated error bars mark the SNR corresponding to the mean and 90% occurrence interval of the backscatter from trees at X band for the (red) HH and (purple) VV polarizations according to the model presented in [38].

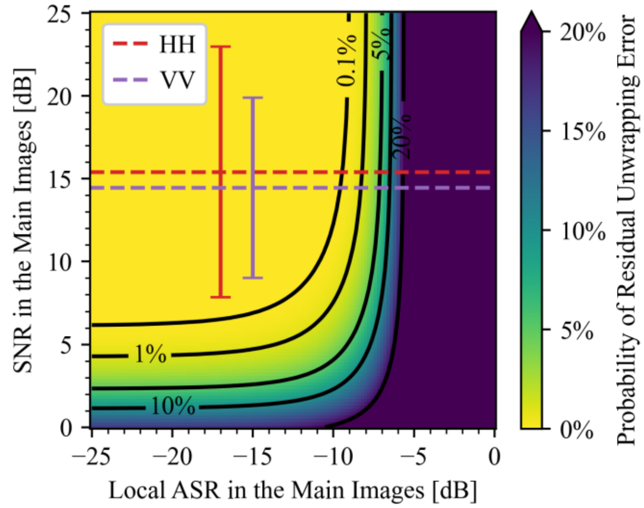

Fig. 10. Average probability of residual unwrapping error as a function of the local ASR and the SNR, both in the images of the main satellites, for the same parameters as Fig. 8, but considering coherent azimuth ambiguities [20] and a CubeSat with a 50 cm square antenna. The horizontal dashed lines and associated error bars mark the SNR corresponding to the mean and 90% occurrence interval of the backscatter from soil and rock at X band for the (red) HH and (purple) VV polarizations according to the model presented in [38].

B. Simulation and Analysis of Results

A CubeSat with a square antenna of length and height of 50 cm is chosen for the simulation that is presented in this subsection. Its peak gain is 11.3 dB lower than that of the antennas of the main satellites. Fig. 11 shows the one-way and two-way antenna patterns in range and azimuth for the images of the main satellites and the CubeSat. Fig. 11 (a) shows that the CubeSat antenna does provide some range ambiguity suppression by having a null located in the first-order ambiguous swath at nearer range. The worst distributed-target RASR across the swath is −25.4 dB for the main satellites and −25.6 dB for the CubeSat. Fig. 11 (b) shows that the CubeSat antenna provides virtually no azimuth ambiguity suppression. The distributed-target AASR is −17.4 dB for the main satellites and −8.1 dB for the CubeSat.

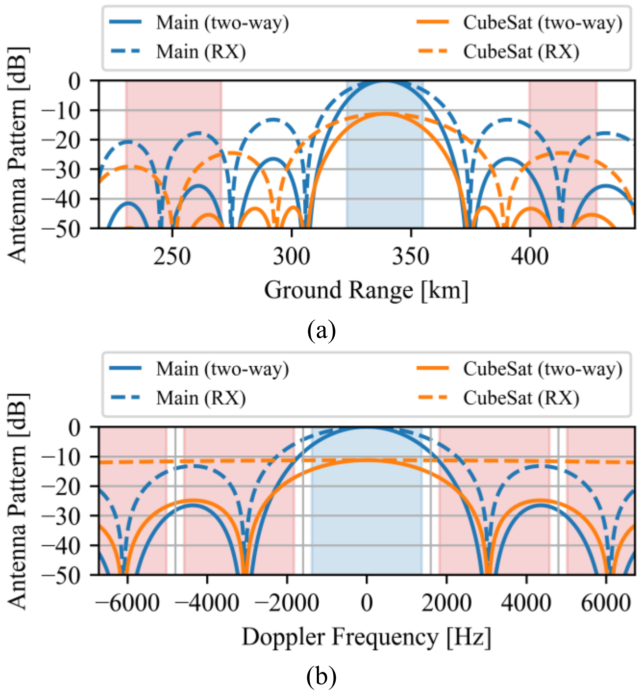

Fig. 11. Receive and two-way antenna patterns of the main satellites and the CubeSat along (a) range and (b) azimuth for the SAR interferometer with a CubeSat add-on described in Table I. The blue and red shaded areas mark, in (a), the main and ambiguous swaths, and, in (b), the processed and ambiguous bandwidths, respectively.

A coregistered pair of images, one of which is shown in Fig. 12 (a), from a TanDEM-X acquisition over an area southwest of Rosenheim, Germany, is used as input for a simulation of the SAR interferometer with the CubeSat add-on on the same area. The beta-naught, the coherence and the height of each pixel are estimated from the input TanDEM-X data, and the images acquired by the SAR interferometer with a CubeSat add-on are simulated from these parameters. The input images were acquired with an incidence angle of 36.2° and have a sample spacing of 2.20 m in azimuth and 1.36 m in slant range. The interferogram formed by the images has a height of ambiguity of 45.2 m. There is a mountainous area in the top of image and more flat terrain in the bottom of the image that also contains forested areas. The beta naught is estimated by filtering the two images with a Lee filter [40]-[42] with a 9 × 9 boxcar window and then computing the mean between the two results. The coherence, shown in Fig. 12 (b), is obtained through the usual estimator [2] with a 7 × 7 boxcar window. To obtain the height of each pixel, an interferogram is formed from the images, then filtered with a Goldstein filter [43], [44] with overlapping 32 × 32 windows and parameter $\alpha = 0.8$, then unwrapped with a minimum cost flow (MCF) algorithm [9], and finally the unwrapped phases are converted to heights. The resulting DEM is shown in Fig. 12 (c).

The simulation is performed for the SAR interferometer whose parameters are listed in Table I with a CubeSat add-on in the first configuration (cf. Fig. 1 (a)). Three images are simulated already coregistered, one for each satellite. The values of each pixel are obtained as the sum of noise and the realization of a zero-mean complex multivariate Gaussian random variable whose parameters are derived from the estimates obtained from the input images. The noise is complex Gaussian with a variance matching the noise-equivalent beta naughts for the images of the main satellites and the image of the CubeSat shown in Table I. The coherence matrix of the random variable has the absolute value of all off-diagonal elements set to the input estimated coherence $|\hat{\gamma}|$ (cf. Fig. 12 (b)). The variance of each of its components is given by the input estimated beta naught $\widehat{\beta^0}$, and the expectation values of the interferometric phases are set corresponding to the height $\hat{h}$ of the input DEM (cf. Fig. 12 (c)) and the heights of ambiguity derived from the baselines between the satellites while also not considering the flat Earth phase:

$$\begin{gathered}\begin{bmatrix} q_1 \\ q_2 \\ q_3 \end{bmatrix} \sim \mathcal{CN}\left(\begin{bmatrix} 0 \\ 0 \\ 0 \end{bmatrix}, \begin{bmatrix} 1 & |\hat{\gamma}| & |\hat{\gamma}| \\ |\hat{\gamma}| & 1 & |\hat{\gamma}| \\ |\hat{\gamma}| & |\hat{\gamma}| & 1 \end{bmatrix}\right), \\ \begin{bmatrix} u_1 \\ u_2 \\ u_3 \end{bmatrix} = \sqrt{\widehat{\beta^0}} \begin{bmatrix} 1 & 0 & 0 \\ 0 & e^{j\frac{2\pi\hat{h}}{HoA_L}} & 0 \\ 0 & 0 & e^{j\frac{2\pi\hat{h}}{HoA_S}} \end{bmatrix} \begin{bmatrix} q_1 \\ q_2 \\ q_3 \end{bmatrix} + \begin{bmatrix} n_1 \\ n_2 \\ n_3 \end{bmatrix},\end{gathered} \tag{11}$$

where u_1, u_2, and u_3 are the values of the simulated images corresponding, respectively, to the two main satellites and the CubeSat, n_1, n_2, and n_3 are the noises added to each image and HoA_L and HoA_S are the heights of ambiguity corresponding, respectively, to the large- and small-baseline interferograms. Note that the coherence used as input to the simulation already contains an SNR decorrelation component and, therefore, introduces additional noise in the simulation. This has little impact in the CubeSat image, because its simulated noise is much stronger than the one coming from the input coherence. Note also that this approach ignores the different volume decorrelation due to the baselines in the simulated system being different from the one of the input data. In a real acquisition, the small-baseline interferogram would contain less volume decorrelation than what is simulated and, therefore, achieve better unwrapping correction performance. One the other hand, the volume decorrelation in the large-baseline interferogram would be stronger, which, however, has little impact on the performance of the unwrapping correction. The three images are then filtered in range and azimuth according to the bandwidths shown in Table I. The two first-order azimuth ambiguities are simulated by shifting the simulated images along azimuth and scaling their amplitude by −20.5 dB and −12.1 dB in the images of the main satellites and the CubeSat, respectively. These scaling factors are the power ratios derived from integrating the corresponding two-way antenna pattern over the ambiguous and main bandwidths. The shift used was of 1855.5 pixels, i.e., around 4.1 km. Finally, only the central part of the images in azimuth is used. The removed parts contribute as azimuth ambiguities to the central part.

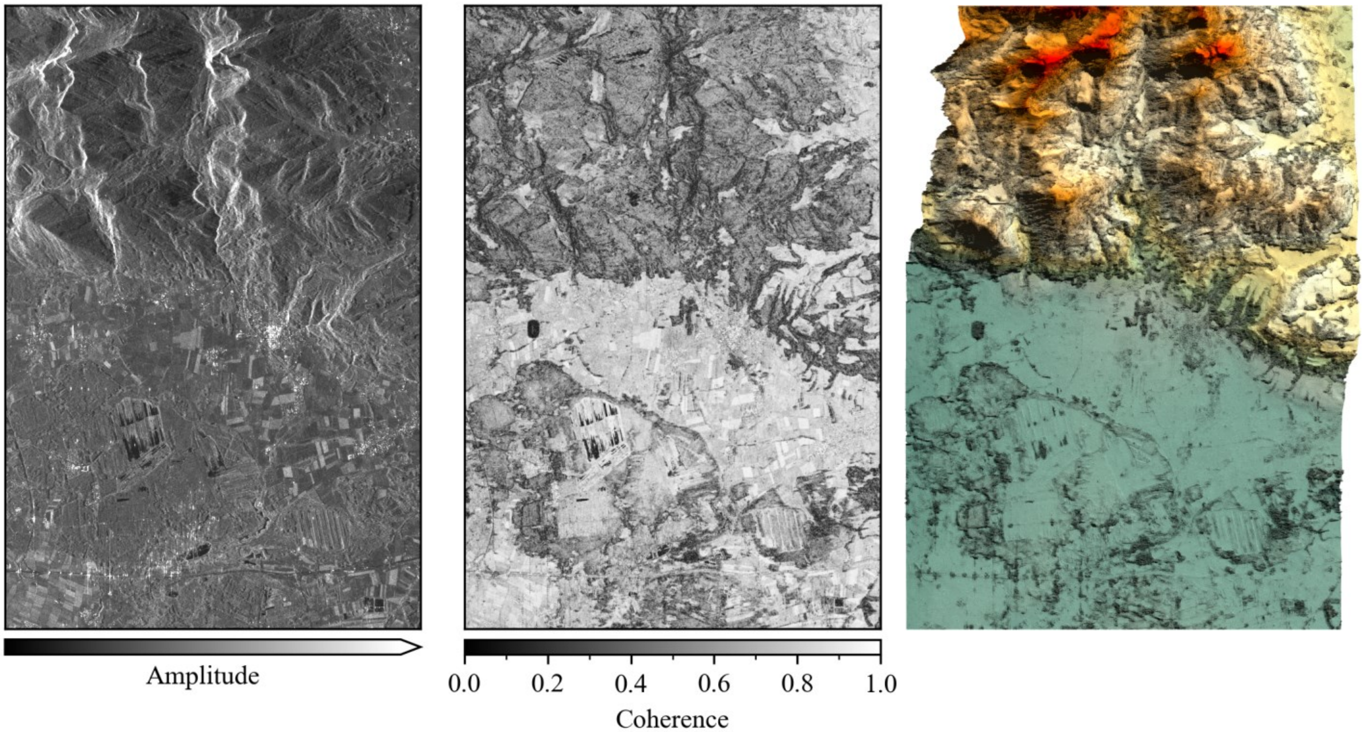

(a) (b) (c)

Fig. 12. (a) One of the images of the pair of coregistered images from a TanDEM-X acquisition over an area southwest of Rosenheim, Germany, used as input for the simulation presented in this section, (b) the estimated coherence of the interferogram formed from the images, and (c) the DEM resulting from filtering and then unwrapping the interferogram.

The large-, medium-, and small-baseline interferograms are then formed by combining the three simulated images, two at a time, and are multilooked by a moving average with a 5×5 boxcar window for the large-baseline interferogram and a 7×7 boxcar window for the medium- and small-baseline interferograms. Note that, due to the processing filters in range and azimuth, the effective number of looks is smaller than the number of pixels in the multilooking windows employed. The interferograms after multilooking are shown in Fig. 13 along with their coherences estimated with boxcar windows with the same sizes as used for the multilooking, the DEMs obtained by unwrapping the interferograms, and their errors with respect to the true terrain height. The histograms of these height errors are shown in Fig. 14. Many unwrapping errors are visible in the large- and medium-baseline DEMs. The small-baseline DEM only presents some unwrapping errors, mostly on the foreshortening areas of the mountainous region, but, as expected, it has a much larger height variance than the large- or medium-baseline interferograms.

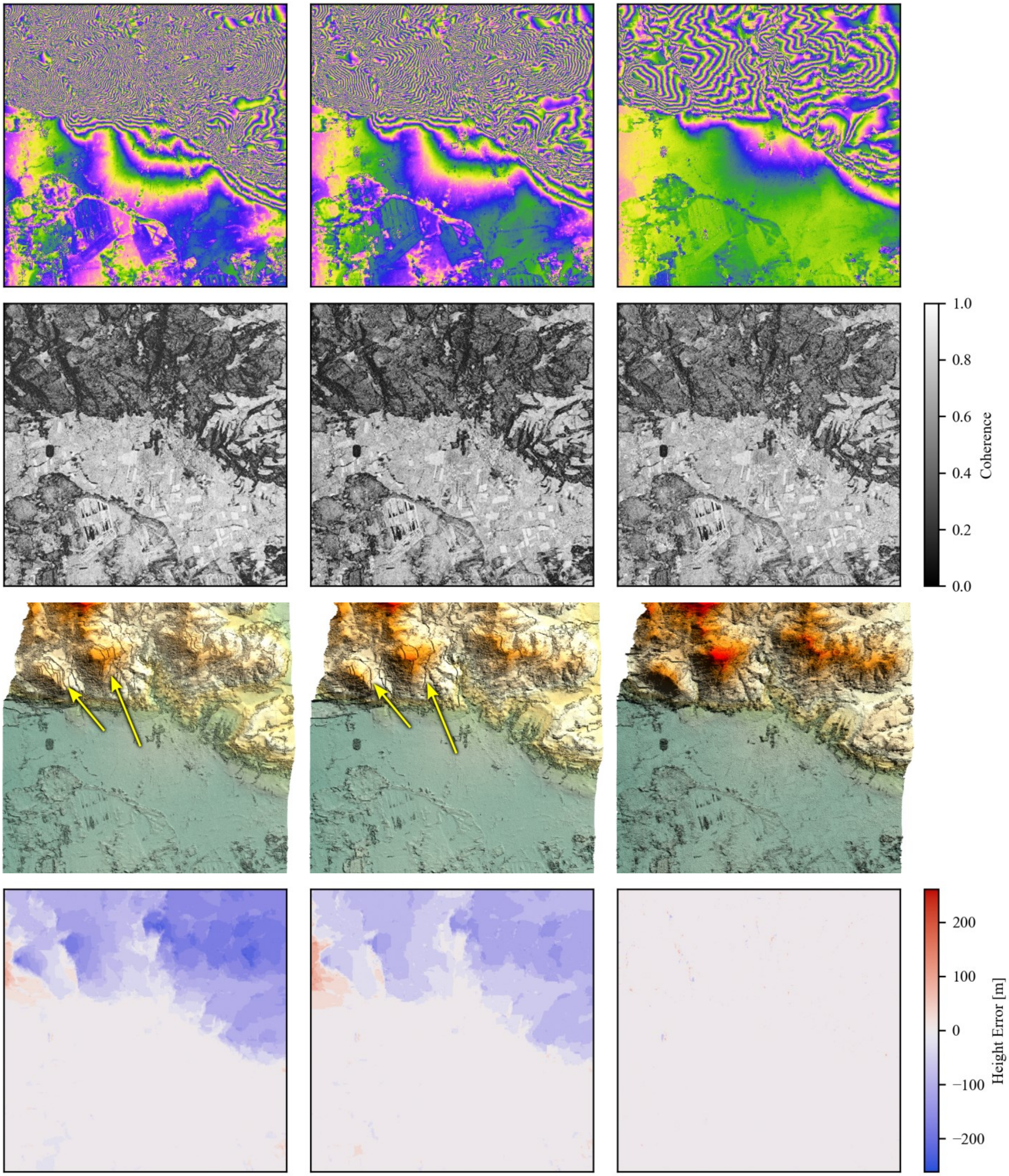

Fig. 13. (first row) Multilooked interferograms formed from the simulated images, (second row) the estimated coherences of the interferograms, (third row) the DEMs resulting from unwrapping the interferograms, and (fourth row) the height errors of the DEMs with respect to the true terrain height, each for the (left column) large, (center column) medium, and (right column) small baselines. The yellow arrows in the large- and medium-baseline DEMs indicate some height discontinuities typical of phase unwrapping errors.

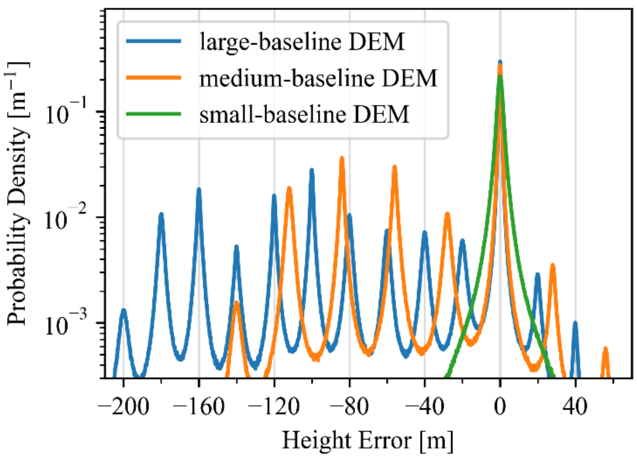

Fig. 14. Histograms of the error of the (blue) large-, (orange) medium-, and (green) small-baseline DEMs shown in Fig. 13 with respect to the true height of the terrain.

A mask of detections of phase unwrapping errors is formed by comparing the large-baseline DEM with the medium- and small-baseline DEMs according to (2) and (3), respectively. The result is shown in Fig. 15 (a). This mask is then smoothed using the DBSCAN clustering algorithm [28] with Eps-neighborhood of radius 5 under the Manhattan metric and a minimum of 8 neighbors for classification as a core point. The smoothed mask is built as the union of the Eps-neighborhoods of all core and border pixels. The result is presented in Fig. 15 (b) and successfully detected 99.98% of the unwrapping errors in the large-baseline DEM. The mask before smoothing contains many "noisy" areas. The smoothing fixes these areas by transforming them into areas uniformly classified as containing unwrapping errors. Furthermore, if the large-baseline DEM were only compared with medium-baseline one, through (2), and not also with the small-baseline one, through (3), some large areas with unwrapping errors would not be detected. These areas are caused by the unwrapping errors in the large- and medium-baseline DEMs adding or subtracting approximately the same height to each, such that the height difference between the DEMs falls below the detection threshold. This effect can be seen clearly in the histogram of height error shown in Fig. 14 by the perfect alignment of peaks of the distributions at −140 m, and by close alignments at −80 m and −60 m. These unwrapping errors are detected by comparison to the small-baseline DEM, through (3), with a detection threshold of 60 m, 3 times the large-baseline height of ambiguity.

The small-baseline DEM is used as reference to correct the phase unwrapping errors in the large-baseline one (cf. Fig. 16 (a)) according to (1) to generate the final DEM, shown in Fig. 17. It has the same resolution and height variance as the large-baseline DEM. The residual unwrapping errors present in it are shown in Fig. 16 (b). Fig. 18 (a) shows how these unwrapping errors are distributed with respect to the estimated coherence of the large-baseline DEM, revealing that they mostly appear in low-coherence regions. 96% of the residual unwrapping errors occur in pixels where the coherence is smaller than 0.4 in the large-baseline interferogram. Fig. 18 (b) presents the percentage of residual unwrapping errors as a function of the coherence of the large-baseline interferogram, showing that the rate of residual unwrapping errors is 0.1% or less for areas whose estimated coherence is larger than 0.6 in the large-baseline interferogram. The overall percentage of residual unwrapping errors is 0.27%, 0.07%, and 0.02% in the areas with estimated coherences larger than 0.4, 0.5, and 0.6 in the large-baseline interferogram, respectively. Finally, the fact that the unwrapping correction is not performed in areas where unwrapping errors are not detected prevents the correction from introducing residual unwrapping errors in 0.11% of the pixels in these areas.

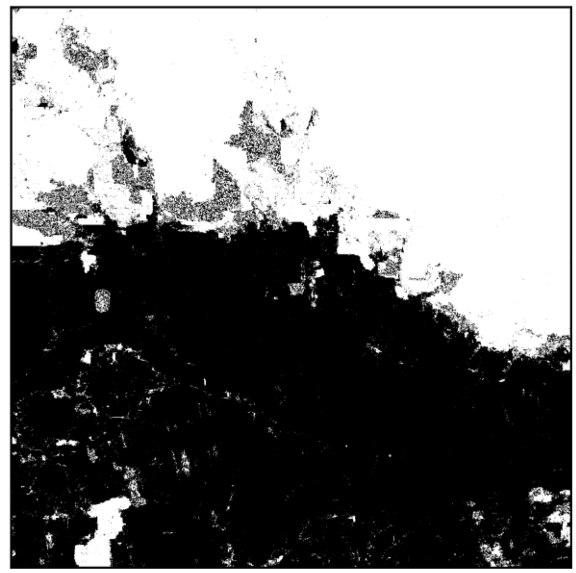

(a)

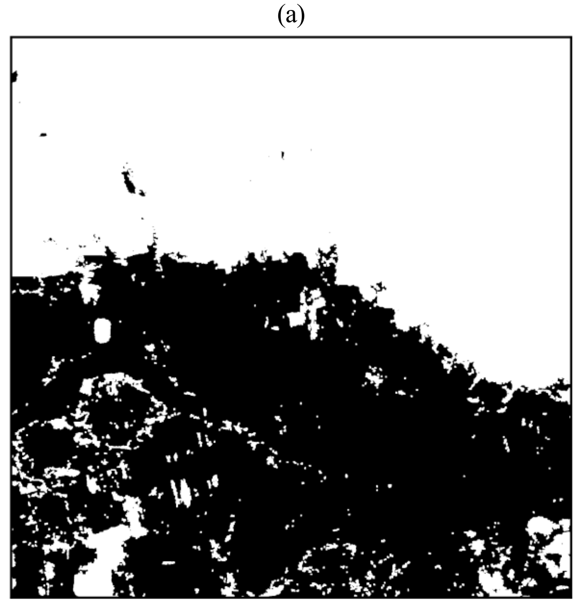

(b)

Fig. 15. (a) mask of detections of unwrapping errors obtained by pixelwise comparing the large-baseline DEM with the medium- and small-baseline DEMs according to (2) and (3), respectively, and (b) the result of smoothing this mask. The white pixels represent detections of unwrapping errors.

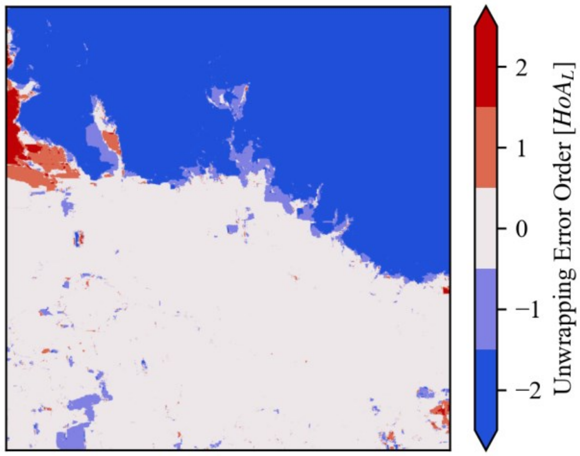

(a)

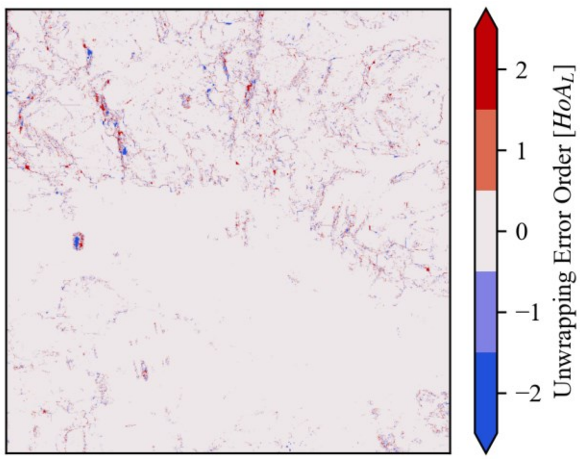

(b)

Fig. 16. Map of (a) unwrapping errors in the large-baseline DEM and (b) residual unwrapping errors in the final DEM, which results from correcting the unwrapping errors in the large-baseline DEM through (1) using the small-baseline DEM as reference.

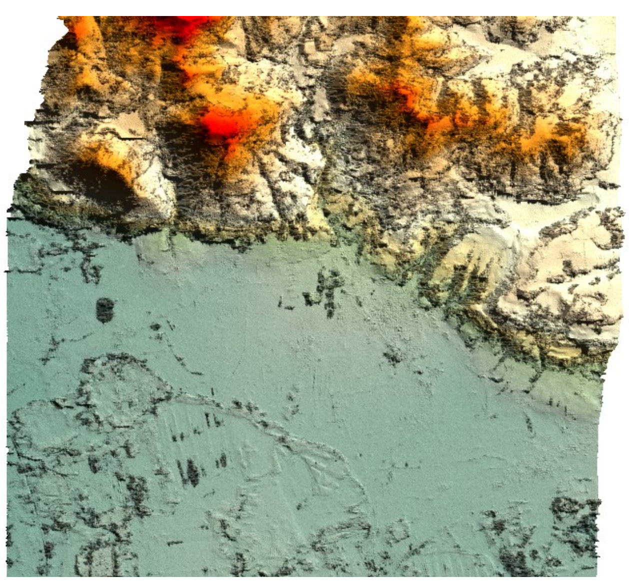

Fig. 17. Final DEM resulting from correcting the phase unwrapping errors in the large-baseline DEM through (1) using the small-baseline DEM as reference.

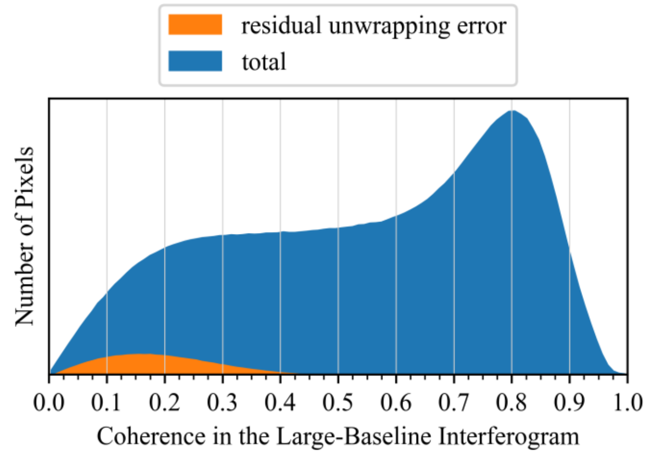

(a)

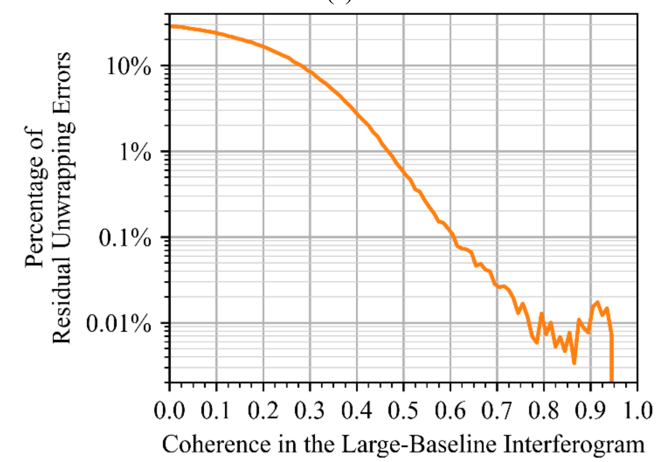

(b)

Fig. 18. (a) (blue) total number of pixels, (orange) number of pixels containing unwrapping errors, and (b) percentage of pixels containing unwrapping errors in the final DEM for varying values of estimated coherence in large-baseline interferogram.

VI. Conclusion and Outlook

A concept based on one or more CubeSat add-ons was proposed that provides information for detecting and resolving phase unwrapping errors in single-pass SAR interferometry without compromising the accuracy or resolution of the final DEM. This is a low-cost approach that allows the monitoring of fast-changing phenomena, due to its capacity of generating DEMs free of unwrapping errors in a single pass of the satellites. Two configurations were proposed for the CubeSats, with the second avoiding the challenging formation flight implied in the first and also having more relaxed requirements for synchronization between the CubeSats and the main satellites. The processing for the phase unwrapping correction was presented along with a theoretical model for its performance that indicates the system is able to resolve phase unwrapping errors with pixelwise probability of failure lower than 0.1% in the example of a CubeSat with a 50 cm square antenna added to a TanDEM-X-like interferometer. The model can also be used in the system design to link requirements on the performance of the unwrapping error correction to requirements on the area of the CubeSat antenna. A simulation based on TanDEM-X data shows that the proposed add-on is successful in correcting unwrapping errors except in areas with very low coherence, such as the foreshortening areas in the mountainous region. Due to the pixelwise nature of the proposed unwrapping correction, residual unwrapping errors may remain in a small percentage of the pixels. However, unwrapping errors generally occur uniformly over large areas, so a non-pixelwise unwrapping correction scheme could further eliminate the sporadic residual unwrapping errors by identifying them as outliers. This work shows that CubeSats can be used to improve the SAR interferometric performance in spite of the low image quality consequent of their small antenna aperture.

While this manuscript tackles the phase unwrapping problem through the concept of a CubeSat add-on, other implementations could be studied, such as extra small receiver antennas attached to satellites with booms that provide a small baseline.

This work also paves the way to distributed single-pass interferometric concepts based on clusters of CubeSats, where a high-quality DEM is obtained from the combination of several low-quality SAR images [45], [46].

ACKNOWLEDGMENT

The authors wish to thank Dr. Francesca Scala for the fruitful discussions and support.

REFERENCES

[1] A. Moreira, P. Prats-Iraola, M. Younis, G. Krieger, I. Hajnsek and K. P. Papathanassiou, “A tutorial on synthetic aperture radar,” in *IEEE Geoscience and Remote Sensing Magazine*, vol. 1, no. 1, pp. 6-43, March 2013, doi: 10.1109/MGRS.2013.2248301.

[2] R. Bamler and P. Hartl, “Synthetic aperture radar interferometry,” *Inv. Probl.*, vol. 14, no. 4, pp. R1–R54, February 1998.

[3] P. A. Rosen et al., “Synthetic aperture radar interferometry,” in *Proceedings of the IEEE*, vol. 88, no. 3, pp. 333-382, March 2000, doi: 10.1109/5.838084.

[4] R. F. Hanssen, *Radar interferometry: data interpretation and error analysis*, Springer, Dordrecht, The Netherlands, 2001.

[5] G. Krieger et al., “TanDEM-X: A Satellite Formation for High-Resolution SAR Interferometry,” in *IEEE Transactions on Geoscience and Remote Sensing*, vol. 45, no. 11, pp. 3317-3341, Nov. 2007, doi: 10.1109/TGRS.2007.900693.

[6] M. Zink et al., “TanDEM-X: 10 Years of Formation Flying Bistatic SAR Interferometry,” in *IEEE Journal of Selected Topics in Applied Earth Observations and Remote Sensing*, vol. 14, pp. 3546-3565, 2021, doi: 10.1109/JSTARS.2021.3062286.

[7] T. G. Farr et al., “The Shuttle Radar Topography Mission”, in *Reviews of Geophysics*, vol. 45, no. 2, 2007, doi: 10.1029/2005RG000183.

[8] H. Yu, Y. Lan, Z. Yuan, J. Xu and H. Lee, “Phase Unwrapping in InSAR: A Review,” in *IEEE Geoscience and Remote Sensing Magazine*, vol. 7, no. 1, pp. 40-58, March 2019, doi: 10.1109/MGRS.2018.2873644.

[9] M. Costantini, “A novel phase unwrapping method based on network programming,” in *IEEE Transactions on Geoscience and Remote Sensing*, vol. 36, no. 3, pp. 813-821, May 1998, doi: 10.1109/36.673674.

[10] M. Lachaise, T. Fritz and R. Bamler, “The Dual-Baseline Phase Unwrapping Correction Framework for the TanDEM-X Mission Part 1: Theoretical Description and Algorithms,” in *IEEE Transactions on Geoscience and Remote Sensing*, vol. 56, no. 2, pp. 780-798, Feb. 2018, doi: 10.1109/TGRS.2017.2754923.

[11] G. Krieger and A. Moreira, “Multistatic SAR Satellite Formations: Potentials and Challenges,” in *IEEE Geoscience and Remote Sensing Symposium*, Seoul, South Korea, July 25-29, 2005, vol. 4, pp. 2680-2684.

[12] E. Peral et al., “Radar Technologies for Earth Remote Sensing From CubeSat Platforms,” in *Proceedings of the IEEE*, vol. 106, no. 3, pp. 404-418, March 2018, doi: 10.1109/JPROC.2018.2793179.

[13] G. di Martino et al., “X-Band SAR Antenna Design for a CubeSat Formation-Flying Remote Sensing Mission,” *2021 IEEE 6th International Forum on Research and Technology for Society and Industry (RTSI)*, 2021, pp. 206-210, doi: 10.1109/RTSI50628.2021.9597211.

[14] A. Renga, A. Gigantino, M. D. Graziano, A. Moccia, A. Fedele and S. Natalucci, “Beamforming and Multi-platform Image Synthesis for RODiO distributed SAR mission,” *73rd International Astronautical Congress (IAC)*, Paris, France, Sep. 2022.

[15] M. Grassi et al, “FORCE: A Formation Flying SAR Based on CubeSat Assemblies,” *73rd International Astronautical Congress (IAC)*, Paris, France, Sep. 2022.

[16] M. N. Peixoto, M. Villano, G. Krieger, and A. Moreira, “Verfahren zur Erkennung und Auflösung von Phasenmehrdeutigkeiten in interferometrischen SAR-Daten,” German Patent Appl. 10 2022 117 088.8, July 8, 2022.

[17] A. Moreira, G. Krieger, and J. Mittermayer, “Satellite configuration for interferometric and/or tomographic remote sensing by means of synthetic aperture radar (SAR),” U.S. Patent 6 677 884 Jul. 1, 2002.

[18] Mittermayer et al., "MirrorSAR: An HRWS Add-On for Single-Pass Multi-Baseline SAR Interferometry," in *IEEE Transactions on Geoscience and Remote Sensing*, vol. 60, pp. 1–18, 2022, Art no. 5224018, doi: 10.1109/TGRS.2021.3132384.

[19] G. Krieger et al., “TanDEM-X: A radar interferometer with two formation-flying satellites,” in *Acta Astronautica*, vol. 89, pp. 83–98, 2013, doi: 10.1016/j.actaastro.2013.03.008.

[20] M. Villano and G. Krieger, "Impact of Azimuth Ambiguities on Interferometric Performance," in *IEEE Geoscience and Remote Sensing Letters*, vol. 9, no. 5, pp. 896–900, Sept. 2012, doi: 10.1109/LGRS.2012.2187271.

[21] J. Mittermayer, G. Krieger, A. Bojarski, M. Zonno, M. Villano, M. Pinheiro, M. Bachmann, S. Buckreuss, A. Moreira, “MirrorSAR: An HRWS Add-On for Single-Pass Multi-Baseline SAR Interferometry,” in *IEEE Transactions on Geoscience and Remote Sensing*, vol. 60, pp. 1-18, 2022, Art no. 5224018, doi: 10.1109/TGRS.2021.3132384.

[22] E. Rodrigues-Silva and M. Rodriguez-Cassola, “Analysis of a POD-based Approach for Phase and Time Synchronization of Bistatic and Multistatic SAR Systems,” *EUSAR 2021; 13th European Conference on Synthetic Aperture Radar*, online, 2021, pp. 1–6.

[23] “Report for Mission Selection: Earth Explorer 10 Candidate Mission Harmony”, European Space Agency, Noordwijk, The Netherlands, ESA-EOPSM-HARM-RP-4129, 2022.

[24] H. Breit et al., “Bistatic synchronization and processing of TanDEM-X data,” in *2011 IEEE International Geoscience and Remote Sensing Symposium*, Vancouver, BC, Canada, 2011, pp. 2424–2427, doi: 10.1109/IGARSS.2011.6049700.

[25] M. Rodriguez-Cassola, “Bistatic Synthetic Aperture Radar Data Processing,” Ph.D. dissertation, Karlsruhe Institute of Technology, Karlsruhe, Germany, 2012.

[26] D. O'Reilly, G. Herdrich, and D. F. Kavanagh, “Electric Propulsion Methods for Small Satellites: A Review,” *Aerospace*, vol. 8, no. 1, p. 22, Jan. 2021, doi: 10.3390/aerospace8010022.

[27] A. Kramer, P. Bangert and K. Schilling, “UWE-4: First Electric Propulsion on a 1U CubeSat—In-Orbit Experiments and Characterization,” *Aerospace*, vol. 7, no. 7, p. 98, Jul. 2020, doi: 10.3390/aerospace7070098.

[28] M. Ester and H. Kriegel and J. Sander and X. Xu, “A density-based algorithm for discovering clusters in large spatial databases with noise”, in *Proc. KDD*, pp. 226-231, 1996.

[29] F. Lombardini and P. Lombardo, “Maximum likelihood array SAR interferometry,” *1996 IEEE Digital Signal Processing Workshop Proceedings*, Loen, Norway, 1996, pp. 358-361, doi: 10.1109/DSPWS.1996.555535.

[30] G. Fornaro, A. M. Guarnieri, A. Pauciullo and F. De-Zan “Maximum likelihood multi-baseline SAR interferometry,” *IEE Proceedings - Radar, Sonar and Navigation*, vol. 153, no. 3, pp. 279–288, Jun. 2006, doi: 10.1049/ip-rsn:20045113.

[31] M. Villano, M. N. Peixoto, N. Ustalli, J. Mittermayer, G. Krieger and A. Moreira, “Decorrelating Ambiguities in SAR Interferometry through Slight PRI Variation,” in *IEEE Transactions on Geoscience and Remote Sensing*, vol. 60, pp. 1-13, 2022, Art no. 5240413, doi: 10.1109/TGRS.2022.3227316.

[32] F. Baselice, G. Ferraioli, V. Pascazio and G. Schirinzi, “Contextual Information-Based Multichannel Synthetic Aperture Radar

Interferometry: Addressing DEM reconstruction using contextual information," in *IEEE Signal Processing Magazine*, vol. 31, no. 4, pp. 59-68, July 2014, doi: 10.1109/MSP.2014.2312282.

[33] I. R. Joughin, D. P. Winebrenner and D. B. Percival, "Probability density functions for multilook polarimetric signatures," in *IEEE Transactions on Geoscience and Remote Sensing*, vol. 32, no. 3, pp. 562-574, May 1994, doi: 10.1109/36.297975.

[34] J. -S. Lee, K. W. Hoppel, S. A. Mango and A. R. Miller, "Intensity and phase statistics of multilook polarimetric and interferometric SAR imagery," in *IEEE Transactions on Geoscience and Remote Sensing*, vol. 32, no. 5, pp. 1017-1028, Sept. 1994, doi: 10.1109/36.312890.

[35] H. A. Zebker and J. Villasenor, "Decorrelation in interferometric radar echoes," in *IEEE Transactions on Geoscience and Remote Sensing*, vol. 30, no. 5, pp. 950-959, Sept. 1992, doi: 10.1109/36.175330.

[36] D. Small, "Flattening Gamma: Radiometric Terrain Correction for SAR Imagery," in *IEEE Transactions on Geoscience and Remote Sensing*, vol. 49, no. 8, pp. 3081-3093, Aug. 2011, doi: 10.1109/TGRS.2011.2120616.

[37] R. Kahle, M. Wermuth, B. Schlepp and S. Aida, "The TerraSAR-X / TanDEM-X Formation Flight: Challenges to Flight Dynamics and First Results," in *4th International Conference on Spacecraft Formation Flying Missions & Technologies*, St-Hubert, Quebec, Canada, May 2011.

[38] F. T. Ulaby and M. C. Dobson, Handbook of Radar Scattering Statistics for Terrain, Artech, 2019.

[39] M. Martone, P. Rizzoli and G. Krieger, "Volume Decorrelation Effects in TanDEM-X Interferometric SAR Data," in *IEEE Geoscience and Remote Sensing Letters*, vol. 13, no. 12, pp. 1812-1816, Dec. 2016, doi: 10.1109/LGRS.2016.2614103.

[40] J. -S. Lee, L. Jurkevich, P. Dewaele, P. Wambacq and A. Oosterlinck, "Speckle filtering of synthetic aperture radar images: A review," in *Remote Sensing Reviews*, vol. 8, pp. 313-340, 1994, doi: 10.1080/02757259409532206.

[41] J. -S. Lee, "Digital Image Enhancement and Noise Filtering by Use of Local Statistics," in *IEEE Transactions on Pattern Analysis and Machine Intelligence*, vol. PAMI-2, no. 2, pp. 165-168, March 1980, doi: 10.1109/TPAMI.1980.4766994.

[42] J. -S. Lee, "Speckle analysis and smoothing of synthetic aperture radar images," in *Computer Graphics and Image Processing*, vol. 17, no. 1, pp. 24-32, 1981, doi: 10.1016/S0146-664X(81)80005-6.

[43] R. M. Goldstein and C. L. Werner, "Radar ice motion interferometry," in *Proc. 3rd ERS Symp.*, vol. 2, Florence, Italy, 1997, pp. 969–972.

[44] R. M. Goldstein and C. L. Werner, "Radar interferogram filtering for geophysical applications," in *Geophys. Res. Lett*., vol. 25, no. 21, pp. 4035–4038, 1998, doi: 10.1029/1998GL900033.

[45] M. N. Peixoto, M. Villano, G. Krieger, and A. Moreira, "Method for generating digital elevation models of a to-be considered region on earth by using a system of multiple synthetic aperture radar (SAR) platforms," German Patent Appl. 10 2023 118 442.3, July 12, 2023.

[46] M. N. Peixoto, M. Villano, G. Krieger, A. Moreira, and C. Waldschmidt, "A Novel Technique to Generate Digital Elevation Models in a Single Pass Using a Cluster of Smallsats," in *2023 IEEE International Geoscience and Remote Sensing Symposium*, Pasadena, CA, USA, 2023, pp. 8331–8334.